ELSEVIER

Contents lists available at ScienceDirect

Earth and Planetary Science Letters

www.elsevier.com/locate/epsl



Diffusion rates of hydrogen defect species associated with site-specific infrared spectral bands in natural olivine



Yang (Will) Li, Stephen J. Mackwell*, David L. Kohlstedt

Department of Earth Sciences, University of Minnesota, Minneapolis, MN 55455, USA

ARTICLE INFO

Article history:
Received 26 May 2021
Received in revised form 20 December 2021
Accepted 28 January 2022
Available online xxxx
Editor: R. Dasgupta

Keywords: olivine diffusion infrared hydrogenation dehydrogenation anisotropy

ABSTRACT

We investigated hydrogen transport in naturally occurring, iron-bearing samples of San Carlos olivine that were hydrogenated at confining pressures of 200 or 300 MPa and 1173 to 1303 K or dehydrogenated at room pressure and 1191 to 1358 K. Chemical diffusion coefficients were determined from diffusion profiles for individual O-H-stretching bands from series of infrared spectra in orthogonal directions across each sample. Within experimental uncertainty, the diffusivities associated with all the individual bands are in good agreement with one another in both the hydrogenation and the dehydrogenation experiments. Hydrogenation proceeds by two diffusion mechanisms, as reported previously. The faster process involves interstitial diffusion of protons coupled with a counter-flux of polarons, with proton diffusion rate-limiting hydrogenation. For this mechanism, diffusion is faster along the olivine [100] direction than along [010] and [001], consistent with the anisotropy reported for proton diffusion and conductivity in olivine. The slower process involves interstitial proton diffusion coupled with a parallel flux of metal vacancies, with vacancy diffusion rate-limiting hydrogenation. For this mechanism, diffusion is faster along [001] than along [100] and [010], consistent with the anisotropy previously reported for the diffusion of metal cations in olivine. Diffusivities from our new dehydrogenation experiments are identical in both magnitude and anisotropy to those determined in our earlier hydrogenation experiments. This agreement demonstrates the validity of studies that used the results of our hydrogenation experiments to analyze dehydrogenation profiles in olivine xenocrysts and olivine in mantle xenoliths to determine rates of magma ascent from the source regions in Earth's interior.

© 2022 Elsevier B.V. All rights reserved.

1. Introduction

The incorporation of a small amount of water (hydrogen) in nominally anhydrous minerals (NAMs) profoundly influences the kinetic properties of the materials that comprise Earth's upper mantle, including viscosity (e.g., Kohlstedt, 2006; Karato, 2010), electrical conductivity (e.g., Karato, 2006), ionic diffusion (e.g., Chakraborty, 2010; Costa and Chakraborty, 2008), elastic properties (e.g., Jacobsen et al., 2008), and attenuation of seismic waves (e.g., Karato, 2003). Since olivine is the most abundant mineral in Earth's upper mantle, the mechanism of incorporation of water in olivine and the associated alteration of its point defect chemistry has been the subject of numerous studies and vigorous debate over the last three decades.

Although most hydrogen ions are bonded to oxygen ions in olivine and observed as O-H (hydroxyl) stretching bands in infrared spectra, the specific mechanisms by which hydrogen is in-

* Corresponding author.

E-mail address: sjmackwell@gmail.com (S.J. Mackwell).

corporated into the lattice remains under discussion. Studies have focused on the dependence of water solubility on various thermodynamic parameters (e.g., Bai and Kohlstedt, 1992, 1993; Kohlstedt et al., 1996; Mosenfelder et al., 2006; Withers and Hirschmann, 2008; Kovács et al., 2010; Gaetani et al., 2014). These analyses provide some insight into the mechanisms of water incorporation under water-saturated conditions.

Processes of hydrogen diffusion in olivine are not fully understood. On the one hand, knowledge of the mechanisms by which hydrogen diffuses in olivine can help in understanding the hydrogenation process that leads to a water-saturated condition and thus interpretation of the observed dependence of the water solubility on specific thermodynamic parameters. On the other hand, under most thermochemical conditions in Earth's mantle, rocks are not water saturated (e.g., Peslier, 2010) and are constantly undergoing dynamic hydrogen exchange with the ambient environment, such as in the transition zone and at the lithosphereasthenosphere boundary (Hirschmann, 2006; Green et al., 2010; Karato, 2011). Thus, it is of great importance to determine the kinetics of hydrogen transport and the mechanisms of hydrogen diffusion into and out of olivine grains.

Numerous studies have investigated the speciation of individual hydroxyl bands in the infrared spectra of natural and synthetic olivine, both untreated and after hydrothermal experiments, since the early work of Beran and Putnis (1983) and Miller et al. (1987). Theoretical ab initio and molecular dynamics techniques have been used to correlate individual defects within olivine and forsterite with bands in the infrared spectra (e.g., Wright and Catlow, 1994; Brodholt and Refson, 2000; Braithwaite et al., 2003; Balan et al., 2011; Umemoto et al., 2011; Crépisson et al., 2014). Additional studies have focused on the nature of the hydrogen-bearing defects in natural olivine, synthetic forsterite, and synthetic Ti-doped forsterite using anisotropy of infrared hydroxyl bands and/or carefully controlled thermochemical environments during hydrothermal experiments (e.g., Libowitzky and Beran, 1995; Matveev et al., 2001; Lemaire et al., 2004; Berry et al., 2005, 2007; Walker et al., 2007; Kovács et al., 2010; Padrón-Navarta et al., 2014; Tollan et al., 2017, 2018; Padrón-Navarta and Hermann, 2017; Le Losq et al., 2019; Jollands et al., 2019; Demouchy and Alard, 2021). These studies have suggested a range of substitution mechanisms in synthetic forsterite and natural olivine, including protons associated with Si vacancies, protons associated with metal vacancies, protons involved with titanium substitution, and protons associated with trivalent cations, including iron. Le Losq et al. (2019) summarized prior analyses and identified the hydroxyl bands in the range 3500 to 3630 cm⁻¹ as due to protons associated with silicon vacancies, those in the range 3300 to 3400 cm⁻¹ as due to defect associates formed between protons in metal vacancies coupled to trivalent ions in metal sites, and those around 3200 cm⁻¹ as due to protons associated with metal vacancies.

Early measurements of the diffusion of hydrogen ions in natural olivine were performed by Mackwell and Kohlstedt (1990) and Kohlstedt and Mackwell (1998), with additional later experiments by Demouchy and Mackwell (2006). After a hydrothermal anneal, these studies determined the concentration of hydrogen as a function of distance into the olivine crystals through measurement of infrared spectra with an emphasis on the kinetics of the incorporation process rather the speciation of the defect species resulting in the various infrared bands. Two mechanisms for hydrogen transport in olivine were established: 1) a fast mechanism involving exchange of protons and polarons (i.e., electron holes associated with the excess charge on ferric iron ions on an octahedral cation site); and 2) a slower mechanism involving coupled inward diffusion of protons and metal vacancies. In both cases, protons diffuse into olivine due to the chemical potential gradient imposed by the hydrothermal environment. In the sample interior, these protons may react with new and existing defects such as silicon or metal vacancies, generating the variety of hydroxyl bands observed in the infrared spectra. These studies determined the rate-limiting processes for these two mechanisms to be diffusion of hydrogen (as protons) and diffusion of metal vacancies, respectively, based on consistency with prior studies of polaron and metal vacancy transport in natural olivine (e.g., Sato, 1986; Mackwell et al., 1988).

These early experiments focused on the hydrogen-related defects that were introduced during hydrothermal treatment for short times at modest temperatures, such that hydrogen concentration profiles could be measured. As experiments for longer times and/or at higher temperatures are needed to equilibrate the samples to the external hydrothermal environment, the defect populations in the samples used for these hydrogenation experiments will be different from fully hydrogenated and equilibrated samples and from natural samples containing hydrogen-related defects. Thus, it is possible that diffusion processes for dehydrogenation may differ from those observed during hydrogenation.

Several recent experimental studies have focused on dehydrogenation of natural olivine (e.g., Jollands et al., 2019; Ferriss et al., 2018; Barth et al., 2019), with results that are generally consistent

with the earlier hydrogenation experiments, though there are differences in absolute diffusivities for protons and metal vacancies among olivine samples from different locations. During dehydrogenation experiments, defect associates such as $(2H)_{\rm Me}^{\times}$ and $(4H)_{\rm Si}^{\times}$ must be disassociated to liberate protons that can then diffuse rapidly toward the surface of the sample; the defect notation follows that of Kröger and Vink (1956). Jollands et al. (2016, 2019) argued that decreases in the peaks associated with silicon vacancies in natural olivine and synthetic forsterite result from reactions in which protons dissociate from silicon vacancies and move into a faster diffusion pathway that may involve coupled transport with metal vacancies. Similarly, He et al. (2021) noted that hydrogen trapped at metal vacant sites is less tightly bound than hydrogen associated with silicon vacancies.

In their study of hydrogen diffusion in synthetic samples of forsterite and Ti-doped forsterite, Padrón-Navarta et al. (2014) reported a unique diffusivity for each of the site-specific species based on analyses of infrared spectra measured following dehydrogenation experiments. From their results, the infrared bands that they attribute to trivalent cations and metal vacancies exhibited the greatest loss during dehydrogenation, while those that they associate with silicon vacancies had the least loss. They interpreted these results as illustrating that hydrogen associated with silicon vacancies diffuses much more slowly than that associated with metal vacancies. In a reinterpretation of their results, Jollands et al. (2016) argue for a single dominant diffusion process involving protons and metal vacancies, coupled with reactions in which protons dissociate from relatively immobile defect associates in olivine and diffuse coupled to a flux of metal vacancies.

The studies by Padrón-Navarta et al. (2014) and Ferriss et al. (2015) raised questions about whether the earlier work of Mackwell and Kohlstedt (1990), Kohlstedt and Mackwell (1998), and Demouchy and Mackwell (2006), which investigated spatial variance in total hydroxyl content, had adequately addressed any site-specific differences in diffusivities during the hydrogenation of their natural olivine samples. In addition, there remains the question of whether the kinetics and speciation of diffusing defects are equivalent in hydrogenation and dehydrogenation experiments.

In the present study, we analyzed diffusion data from hydroxyl profiles in natural olivine samples subjected to conditions driving either hydrogenation or dehydrogenation in order to address the question of the nature of the diffusing hydrogen species in natural olivine. The hydrogenated samples were previously studied by Mackwell and Kohlstedt (1990), Kohlstedt and Mackwell (1998), and Demouchy and Mackwell (2006), who measured the total hydroxyl content by integrating across all infrared bands from 3250 to 3650 cm⁻¹. We reanalyzed the spectra for a subset of these samples by calculating the hydroxyl concentration as a function of position parallel to the three diffusion directions for each hydroxyl band in the spectrum as well as recalculating the total hydroxyl concentration from the full hydroxyl spectrum as a function of position. In addition, new experiments were performed to investigate dehydrogenation of previously hydrated samples to determine if the kinetics of hydrogenation and dehydrogenation are the same for both the full hydroxyl spectrum and for groups of individual bands. These new measurements thus permit an examination of the appropriateness of using diffusivities determined from hydrogenation experiments to calculate rates of magma ascent from dehydrogenation profiles of olivine xenocrysts and xenolithic olivine grains.

2. Hydrogen diffusion experimental methods

Naturally occurring single crystals of iron-bearing San Carlos (Arizona, USA) olivine with no cracks or optically visible inclusions were prepared for hydrogen diffusion experiments. The crystals

Sample	Type	T (K)	P (MPa)	<i>t</i> (h)	f_{O_2}	$[100] \times [010] \times [001]$ (mm ³)
SC14-6	Hydro	1173	300	1.0	Fe/FeO	3.32 × 4.07 × 3.19
SC16-4	Hydro	1273	300	0.6	Ni/NiO	$2.84 \times 5.03 \times 3.23$
SC31-2	Hydro	1173	200	21.1	Ni/NiO	$2.82 \times 4.72 \times 3.38$
SC31-3	Hydro	1273	200	8.0	Ni/NiO	$2.82 \times 4.76 \times 3.02$
SC31-5	Hydro	1303	200	5.0	Ni/NiO	$2.70\times4.03\times2.82$
PI-1918-3	Dehydro*	1191	0.1	20.0	$\sim \! 10^{-7} \; atm$	1.83 × 2.50 × 1.83
PI-1914	Dehydro*	1253	0.1	5.0	$\sim \! 10^{-7}$ atm	$3.07 \times 4.42 \times 3.65$
PI-1918-1	Dehydro	1322	0.1	3.0	$\sim \! 10^{-7}$ atm	$2.99 \times 0.67 \times 2.28$
PI-1918-2	Dehydro*	1358	0.1	2.0	$\sim 10^{-7}$ atm	$2.71 \times 0.94 \times 2.67$

 Table 1

 Experimental conditions and sample sizes for the hydrogenation (Hydro) and dehydrogenation (Dehydro) experiments.

were orientated using Laue X-ray diffraction, and the orientations were checked with electron backscatter diffraction (EBSD).

2.1. Hydrogenation experiments

For hydrogenation experiments, we investigated in greater detail the spectra of five samples from our previous studies (Mackwell and Kohlstedt, 1990; Kohlstedt and Mackwell, 1998). These samples (SC14-6, SC16-4, SC31-2, SC31-3, and SC31-5) were cut with faces perpendicular to each of the crystallographic axes $(\pm 5^{\circ})$ and polished using diamond lapping films from 30 to 0.5 μ m. Samples sizes were roughly 3 \times 5 \times 3 mm³ parallel to the olivine [100], [010], and [001] crystallographic axes, respectively. FTIR analyses were performed to confirm the dry state of the samples prior to hydrogenation experiments.

Samples SC14-6 and SC16-4 were hydrothermally annealed for relatively short times of ≤ 1 h in iron or nickel capsules at temperatures of 1173 and 1273 K, respectively, and a confining pressure of 300 MPa in a gas-medium pressure vessel. Oxygen fugacity was buffered by Fe/FeO or Ni/NiO. Silica activity was buffered by a mixture of olivine plus orthopyroxene powders. Samples SC31-2, SC31-3, and SC31-5 were hydrothermally annealed for longer times of ≥ 5 h in platinum capsules at temperatures of 1173 to 1303 K and a confining pressure of 200 MPa in cold-seal pressure vessels. Oxygen fugacity was buffered by Ni/NiO powders. Silica activity was buffered by orthopyroxene powder. Experimental conditions are summarized in Table 1.

At the end of each experiment, temperature was decreased at a constant pressure to 973 K at $\sim\!150$ K/min, and then decreased to room temperature at $\sim\!30$ K/min. The fast initial cooling rate was used to prevent the formation of secondary hydrous phases and limit the precipitation of the hydrous defects as fluid inclusions (Mackwell et al., 1985; Kohlstedt and Mackwell, 1998). Metal capsules were pierced to verify that water was present throughout each experiment.

2.2. Dehydrogenation experiments

For the dehydrogenation experiments, the first step was to obtain water-saturated olivine single crystals with a uniform distribution of hydrogen throughout the samples. Olivine single crystals PI-1914, PI-1918-1, PI-1918-2, and PI-1918-3 were pressed with talc and brucite (2:1 by weight) and 10 to 14 drops of distilled water into cylindrical nickel capsules with an inner diameter of 12 mm and a length of 20 mm. A nickel disc was then laser welded onto each end of the capsule to prevent direct loss of water. Hydrothermal anneals were carried out at 1473 K and 300 MPa for 5 h using a gas-medium apparatus (Paterson, 1990). Water-saturation was confirmed with FTIR spectra that revealed a uniform hydroxyl content along all three crystallographic axes.

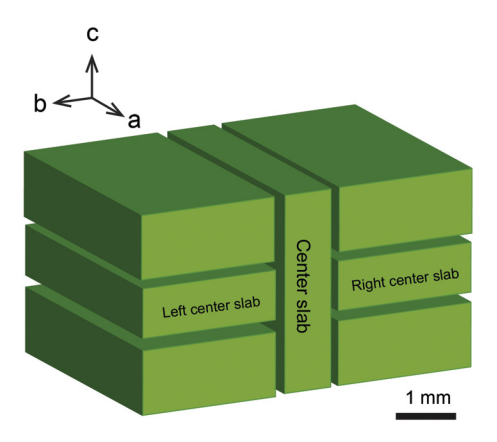


Fig. 1. Schematic of an olivine sample cut into slices for infrared measurements.

The dehydrogenation experiments involved annealing the samples of water-saturated olivine in a one-atmosphere furnace with a thermocouple monitoring the temperature at the sample. Temperature was set within the range 1191 to 1358 K. The experimental conditions for each of four samples are summarized in Table 1. Oxygen fugacity was set at $\sim\!10^{-7}$ atm with a flowing mixture of CO and CO $_2$ and monitored with an oxygen fugacity sensor. Samples were quickly retracted from the hot zone of the furnace at the end of experiments and cooled to room temperature.

3. Analytical methods for chemical diffusion profiles

3.1. Fourier transform infrared spectroscopy

Samples from both hydrogenation and dehydrogenation experiments were cut perpendicular to [010] to extract the center slab with [010] as the normal vector, as illustrated schematically in Fig. 1. Chemical diffusion profiles along [100] and [001] were generated by collecting infrared spectra across the middle of the sample from one edge to the other for each direction. The other two slabs from the side slices of the previous cutting step were cut perpendicular to the [001] direction (Fig. 1) to obtain hydrogen diffusion profiles along [010].

The hydroxyl distribution within samples was analyzed using Fourier transform infrared (FTIR) spectroscopy. Infrared spectra were collected over the wavenumber range 2000 to 4000 cm $^{-1}$ with a Bruker $^{\text{TM}}$ IFS 120 HR high resolution FTIR spectrometer coupled with a Bruker $^{\text{TM}}$ IR microscope and a KBr beam splitter. For the hydrogenation samples, 200 scans were accumulated for each spectrum at a resolution of 1 cm $^{-1}$. The polarized infrared beam (E // [100]) was focused on a depth near the middle of the sample. Spectra were collected from edge to edge along the center axis of the sample. Such a series of infrared spectra for SC31-3 along the three principal axes is illustrated in Fig. 2. Other aspects of

^{*} Samples had been pretreated hydrothermally at 300 MPa, 1473 K, 5 h, with a Ni/NiO oxygen buffer.

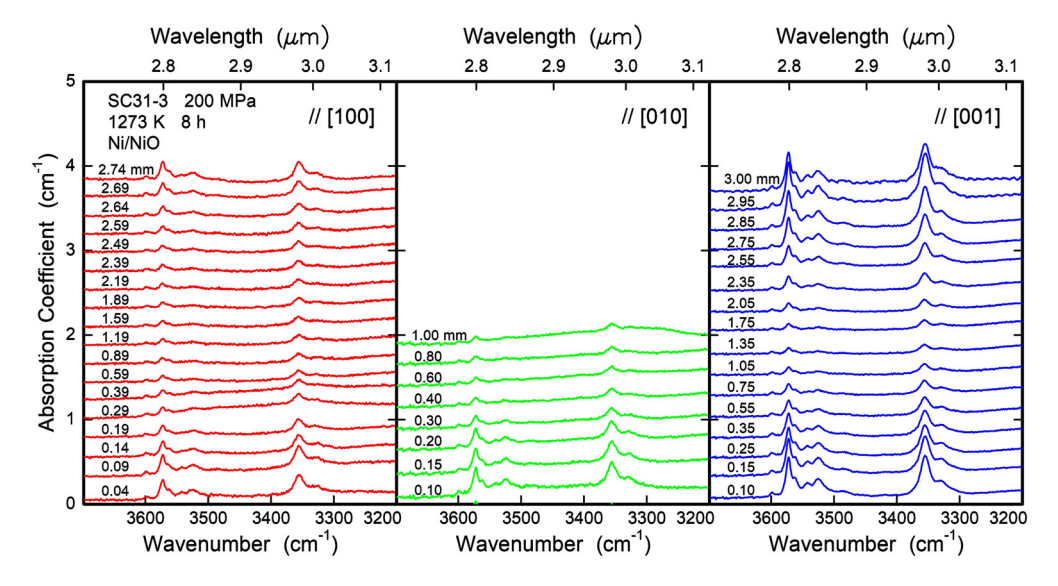


Fig. 2. Series of polarized infrared spectra (E // [100]) for sample SC31-3 as a function of position along the three principal axes. Each spectrum is labeled with the distance of the measurement from the outside edge of the sample. For diffusion parallel to [100] and [001], spectra were measured from one edge of the sample to the other; for [010], spectra were only measured part way from one edge of the sample due to the sectioning procedure.

the technical setup for the spectrometer are identical to those described by Demouchy and Mackwell (2003).

For measurements of the infrared spectra of the dehydrogenation samples, 128 scans were accumulated using the same model of spectrometer and configuration, but with a resolution of 2 cm $^{-1}$ using an unpolarized beam over the wavenumber range of 1000 to 4000 cm $^{-1}$. Since we were not looking specifically at defect speciation, we used unpolarized spectra to maximize the signal-to-noise ratio, especially for the lowest band strengths. A window $20\times200~\mu\text{m}^2$ with the long dimension perpendicular to the profile direction was chosen to minimize the convolution effect due to the gradient in water concentration along the diffusion profile, thus optimizing the signal-to-noise ratio. Air purged of H_2O and CO_2 was flowed into the zone around the sample to limit contamination due to atmospheric moisture. A background spectrum was collected before measurements on samples to remove the interference from any residual moisture in the air.

3.2. Method for fitting individual infrared spectra

Raw infrared spectra were processed with OriginLab® software. Each spectrum was first smoothed using a 20 points Savitzky-Golay filtering method to increase the signal-to-noise ratio. The spectrum was then baseline corrected by fitting the regions away from O-H-stretching bands and normalized to a thickness of 1 cm. Each spectrum was subsequently deconvolved as the summation of a series of bands, each with a Gaussian distribution of the form

$$A = A_0 + \frac{C}{\sigma\sqrt{2\pi}}e^{-\frac{(\nu-\nu_{\rm C})^2}{2\sigma^2}}$$

where ν is wavenumber in cm⁻¹, $\nu_{\rm c}$ is the center wavenumber for each band, A and A_0 are the infrared absorption coefficient and residual background level in cm⁻¹, and C and σ are the integral area and standard deviation of the Gaussian distribution. The total number and the wavenumber of the selected primary bands were identified with the "pick-peak" function in OriginLab® software; the "pick-peak" wavenumber was compared with values reported in previous studies. The wavenumbers of six to nine primary bands were chosen as the input of fitting parameters to obtain optimal fitting results. The center wavenumbers of these bands include 3598, 3572, 3566, 3543, 3525, 3490, 3372,

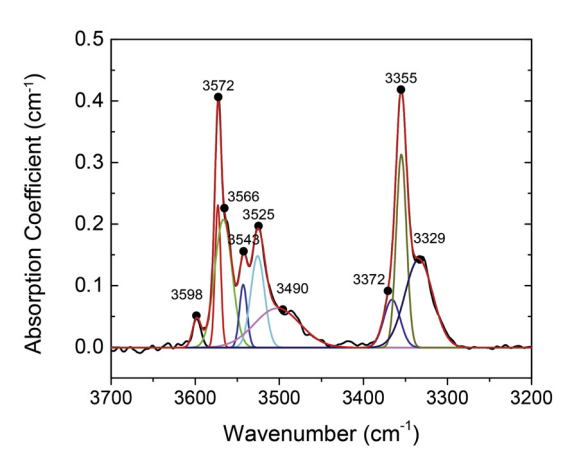


Fig. 3. Example of a fit to the polarized infrared spectrum (E // [100]) of sample SC31-3 with the "pick-peak" function in OriginLab© software, using 9 individual bands and assuming a Gaussian shape for each band.

3355, and 3329 cm⁻¹. An example of fitting the overall spectrum from sample SC31-3 with 9 individual bands, each with a Gaussian distribution, with the wavenumber labeled above each band is provided in Fig. 3. Based on the assignments summarized in Le Losq et al. (2019), the bands identified in this study would result from protons associated with silicon vacancies (3598–3490 cm⁻¹) or protons associated with trivalent ions in/associated with metal vacancies (3372–3329 cm⁻¹). Assessment of the validity of these assignments is beyond the scope of this study.

3.3. Determining the diffusivities for water-derived point defects

The hydroxyl concentration, [OH], associated with each site-specific hydrous defect is proportional to the integrated area *C* (in cm⁻²) under that band in the infrared spectrum. For the purposes of diffusion analysis, the actual value of the proportionality constant is immaterial. Thus, we treat the integrated area under a band in an infrared spectrum as the corresponding hydroxyl concentration. Hydroxyl concentration evolves with time and position according to Fick's second law

$$\frac{\partial C}{\partial t} = \tilde{D}\nabla^2 C,\tag{1}$$

Dallus.						
Sample	T (K)	t (h)	IR band (cm ⁻¹)	$\log \tilde{D}_f // [100]$ $(m^2 s^{-1})$	$\log \tilde{D}_f // [010]$ $(m^2 s^{-1})$	$\log \tilde{D}_f /\!/ [001]$ $(m^2 s^{-1})$
SC14-6	1173	1.0	All 3490 3525 3543 3566 3572	-9.91 ± 0.02 -10.2 ± 0.2 -9.8 ± 0.1 -10.3 ± 0.2 -9.9 ± 0.1 -9.92 ± 0.04	-11.8 ± 0.1 -11.4 ± 0.1 -11.3 ± 0.1 -11.9 ± 0.2 -11.5 ± 0.1 -11.6 ± 0.1	-11.2 ± 0.1 -10.8 ± 0.1 -10.90 ± 0.05 -11.1 ± 0.1 -11.0 ± 0.1 -11.1 ± 0.1
SC16-4	1273	0.6	All 3490 3525 3543 3566 3572	$\begin{array}{c} -9.61 \pm 0.02 \\ -9.78 \pm 0.03 \\ -9.61 \pm 0.02 \\ -9.81 \pm 0.03 \\ -9.64 \pm 0.02 \\ -9.75 \pm 0.03 \end{array}$	$\begin{array}{c} -11.0 \pm 0.1 \\ -11.6 \pm 0.1 \\ -11.9 \pm 0.2 \\ -11.4 \pm 0.2 \\ -11.9 \pm 0.2 \\ -11.8 \pm 0.1 \end{array}$	-11.1 ± 0.1 -10.9 ± 0.1 -11.1 ± 0.1 -11.2 ± 0.1 -11.2 ± 0.1 -11.2 ± 0.1

Table 2aChemical diffusivity data from hydrogenation experiments for the fast diffusion process for each of the infrared bands

where \tilde{D} is the chemical diffusion coefficient and t is time. For a one-dimensional diffusion profile in a hydrogenation experiment, data were fit with the solution to Eq. (1) for an infinite source into a finite slab (Carslaw and Jaeger, 1959) for a short enough time that diffusion from opposite faces did not overlap significantly:

$$C = C_0 + (C_1 - C_0) \times \left\{ \operatorname{erfc}\left(\frac{x}{2\sqrt{\tilde{D}t}}\right) + \operatorname{erfc}\left(\frac{w - x}{2\sqrt{\tilde{D}t}}\right) \right\}, \tag{2}$$

where x is the position parallel to the diffusion direction, w is width of the sample, C_0 is the initial concentration before diffusion, and C_1 is the concentration at the surface of the sample. Values for C_0 and C_1 were obtained by applying a non-linear least squares regression fit to the diffusion profiles using Eq. (2). For the samples from short-duration hydrogenation experiments, C_0 was assumed to be zero since the samples were initially dry; for the longer-duration hydrogenation experiments, C_0 was allowed to vary as the initial concentration included hydrogen defects that had rapidly diffused into the samples prior to the slower incorporation process (Demouchy and Mackwell, 2006). For the samples from dehydrogenation experiments, C_1 was constrained at 0 corresponding to the fully depleted condition at the surface of the sample. After initial independent fits to all diffusion profiles for each sample, values for C_0 and C_1 were set for each sample and the diffusivities for each direction were determined using Eq. (2). since the concentrations at all sample faces should be the same, as should those at the center of all the profiles for each sample.

Interpretation of a measured chemical diffusivity in terms of the rate-limiting process requires understanding the charge coupling condition associated with the diffusion process. Previous studies identified two distinct diffusion processes associated with hydrogen diffusion based on the kinetics and anisotropy of the diffusion of water-derived point defects (Mackwell and Kohlstedt, 1990; Kohlstedt and Mackwell, 1998). At relatively low temperatures and short experimental durations, a fast diffusion process occurs that these authors associated with the counter-diffusion of interstitial protons and polarons; we refer to this process as proton-polaron exchange. At higher temperature and longer experimental durations, a slower diffusion process dominates that was attributed to interstitial proton diffusion coupled with a parallel flux of metal (octahedrally coordinated cation) vacancies; we refer to this process as proton-vacancy coupled diffusion.

Under anhydrous conditions, iron-bearing olivine has a maximum polaron content of ~ 100 molar ppm in one-atmosphere controlled-oxygen-fugacity experiments (Nakamura and Schmalzried, 1983; Tsai and Dieckmann, 1997, 2002); this value sets an upper limit on the amount of hydrogen that can be incorporated through the proton-polaron exchange mechanism. Following

Kohlstedt and Mackwell (1998), the chemical diffusivity, \tilde{D}_f , obtained from the hydroxyl concentration profiles associated with the fast proton-polaron exchange process is given by

$$\tilde{D}_f = \frac{2D_p D_H}{D_p + D_H},\tag{3}$$

where $D_{\rm p}$ is the polaron (h ullet) diffusivity and $D_{\rm H}$ is the interstitial proton (H ullet) diffusivity. Previous measurements by Sato (1986) on the diffusivity of electron holes in olivine parallel to [010] and [001] generated values of $10^{-7.5}$ and $10^{-8.0}$ m 2 /s, respectively, at 1673 K. As these diffusivities are more rapid than the extrapolation of proton diffusion data to this temperature (Kohlstedt and Mackwell, 1998), we assume that $D_{\rm p} \gg D_{\rm H}$ and therefore that $\tilde{D}_f \approx 2D_{\rm H}$.

The slow mechanism involves metal vacancies $(V_{Me}^{//})$ and is referred to as the proton-vacancy coupled diffusion mechanism. In this case, the chemical diffusivity, \tilde{D}_s , is described by

$$\tilde{D}_{s} = \frac{3D_{V_{Me}}D_{H}}{2D_{V_{Me}} + D_{H}},\tag{4}$$

where $D_{V_{Me}}$ is the metal vacancy diffusivity. As the measured values of chemical diffusivity for hydrogen incorporation into natural olivine via this mechanism were observed to be significantly slower than proton diffusion, Kohlstedt and Mackwell (1998) concluded that $D_{H} \gg D_{V_{Me}}$, and thus that $\tilde{D}_{S} \approx 3D_{V_{Me}}$.

4. Chemical diffusivity results

4.1. Proton-polaron exchange process

As noted by Kohlstedt and Mackwell (1998) and Demouchy and Mackwell (2006), hydrogen transport at lower temperatures and shorter times is dominated by exchange of protons from the fluid phase and polarons within the natural olivine crystals. At longer times or higher temperatures, additional hydrogen is incorporated in the olivine through coupled diffusion of interstitial protons and metal vacancies.

We selected two samples for this study (SC14-6, SC16-4) from Mackwell and Kohlstedt (1990) that had been hydrothermally annealed for less than 1 h. Chemical diffusivities calculated from the individual hydroxyl absorption bands (3572, 3566, 3543, 3525, and 3490 cm⁻¹), as well as the full hydroxyl spectrum (all bands) are listed in Table 2a and plotted in Fig. 4. For each diffusion direction in both samples, there is no statistically significant difference in the chemical diffusivities associated with the various hydroxyl bands. Our all-bands diffusivities agree very well with those reported for the same samples by Mackwell and Kohlstedt (1990)

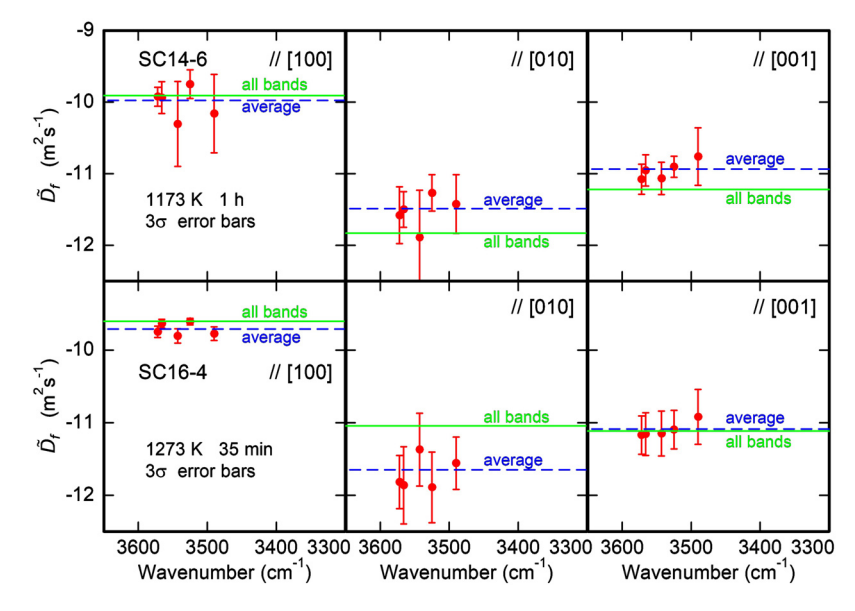


Fig. 4. Chemical diffusivities based on measurements of hydroxyl concentration as a function of position in olivine samples after partial hydrogenation of samples SC14-6 and SC16-4 by the fast proton-polaron exchange process. Dashed lines represent the average of the diffusivities for each band, while solid lines represent the measurement of hydroxyl concentration from the full spectrum.

Table 2b
Chemical diffusivity data from slow hydrogenation experiments for each of the infrared bands.

Sample	T (K)	t (h)	IR band (cm ⁻¹)	$\log \tilde{D}_s // [100]$ $(m^2 s^{-1})$	$\log \tilde{D}_s // [010]$ $(m^2 s^{-1})$	$\log \tilde{D}_s // [001]$ $(m^2 s^{-1})$
SC31-2	1173	21.1	All 3329	-13.76 ± 0.05 -14.4 ± 0.1	-13.65 ± 0.05 -13.75 ± 0.07	-12.35 ± 0.05 -12.26 ± 0.07
			3355	-14.06 ± 0.05	-13.68 ± 0.04	-12.38 ± 0.05
			3372	1 1100 ± 0100	15100 ± 010 1	-12.5 ± 0.3
			3490		-13.40 ± 0.06	-12.7 ± 0.1
			3525	-14.2 ± 0.1	-13.6 ± 0.1	-12.45 ± 0.06
			3543		-13.8 ± 0.1	-12.5 ± 0.1
			3566	-14.1 ± 0.1	-13.60 ± 0.07	-12.54 ± 0.06
			3572	-14.2 ± 0.1	-13.41 ± 0.07	-12.54 ± 0.07
SC31-3	1273	8.0	All	-12.93 ± 0.06	-12.19 ± 0.02	-11.34 ± 0.02
			3329	-12.88 ± 0.05	-12.4 ± 0.1	-11.31 ± 0.06
			3355	-12.78 ± 0.04	-12.3 ± 0.1	-11.40 ± 0.06
			3372	-13.3 ± 0.1	-12.4 ± 0.1	-11.5 ± 0.1
			3490	-13.40 ± 0.05	-12.7 ± 0.2	-11.5 ± 0.1
			3525	-12.79 ± 0.04	-12.4 ± 0.1	-11.33 ± 0.06
			3543	-12.96 ± 0.05	-12.3 ± 0.1	-11.37 ± 0.02
			3566	-12.86 ± 0.03	-12.35 ± 0.05	-11.37 ± 0.02
			3572	-12.87 ± 0.05	-12.3 ± 0.1	-11.42 ± 0.02
			3598	-12.4 ± 0.1	-12.4 ± 0.1	-11.1 ± 0.1
SC31-5	1303	5.0	All	-11.95 ± 0.03		-10.77 ± 0.03
			3329	-12.1 ± 0.1		-10.83 ± 0.04
			3355	-12.07 ± 0.04		-11.03 ± 0.03
			3372			-10.6 ± 0.3
			3490	-11.9 ± 0.1		-10.59 ± 0.05
			3525	-11.96 ± 0.05		-10.88 ± 0.05
			3543	-11.97 ± 0.07		-10.75 ± 0.02
			3566	-11.93 ± 0.05		-10.92 ± 0.05
			3572	-12.01 ± 0.04		-10.92 ± 0.04

and Kohlstedt and Mackwell (1998). For these samples, the chemical diffusion coefficients for diffusion parallel to [100] are significantly larger than parallel to [010] and [001].

4.2. Proton-vacancy coupled diffusion process

4.2.1. Hydrogenation experiments

We selected three samples for this study (SC31-2, SC31-3, and SC31-5) from Kohlstedt and Mackwell (1998) that had been hydrothermally annealed for longer than 5 h. Using the series of infrared spectra for each sample along each of the principal axes,

such as presented for SC31-3 in Fig. 2, we plotted hydroxyl concentration versus position parallel to each axis for the individual hydroxyl absorption bands (3598, 3572, 3566, 3543, 3525, 3490, 3372, 3355, and 3329 $\rm cm^{-1}$), as well as the full hydroxyl spectrum (all bands), as presented for SC31-3 in Fig. 5. The observation that the hydroxyl concentration profiles follow an error function form is strongly indicative of diffusion control of the transport process, rather than reaction or interface control.

Chemical diffusivities calculated from the individual hydroxyl absorption bands, as well as the full hydroxyl spectrum (all bands), are listed in Table 2b and plotted in Fig. 6. As for the proton-

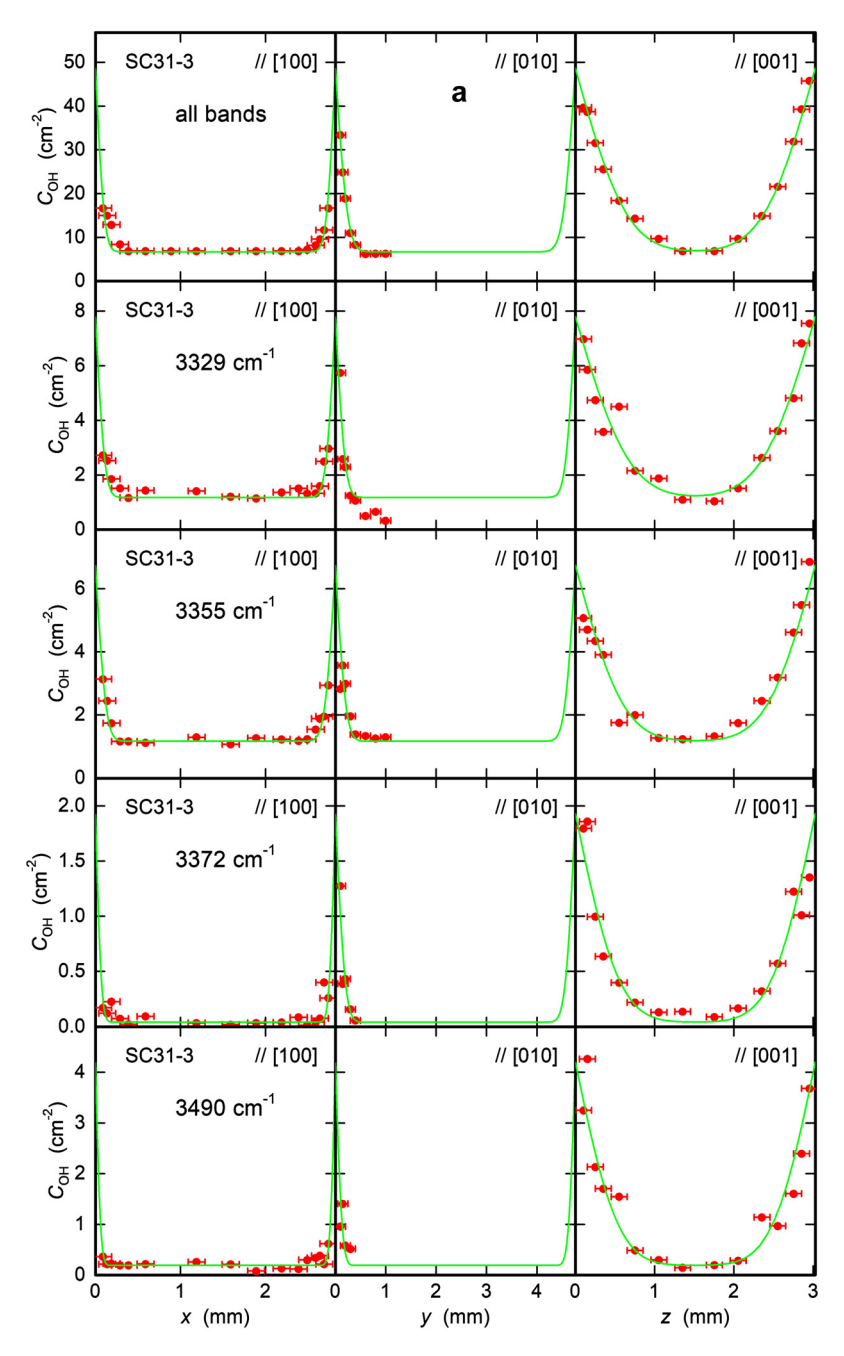


Fig. 5. Hydrogenation diffusion profiles for sample SC31-3 obtained for a) all infrared absorption bands combined and individual bands at 3329, 3355, 3372, and 3490 cm⁻¹ and for b) individual bands at 3525, 3543, 3566, 3572, and 3598 cm⁻¹ for the three orthogonal diffusion directions.

polaron exchange process, each diffusion direction in these samples shows no statistically significant differences in the chemical diffusivities obtained for the various hydroxyl bands. Our all-bands diffusivities agree very well with those reported for the same samples by Kohlstedt and Mackwell (1998) and Demouchy and Mackwell (2006). In contrast to the shorter-duration experiments, the largest values for chemical diffusivity are associated with diffusion parallel to [001], with significantly slower diffusion along [100] and [010]. It is noteworthy that this anisotropy with the fastest diffusion direction parallel to [001] is consistent with prior studies of diffusion processes in natural olivine and synthetic forsterite rate limited by the diffusion of metal vacancies (e.g., Chakraborty, 1997; Dohmen et al., 2007; Dohmen and Chakraborty, 2007; Jollands et al., 2016, 2020).

4.2.2. Dehydrogenation experiments

Chemical diffusion profiles were obtained for samples from dehydrogenation diffusion experiments (PI-1914, PI-1918-1, PI-1918-2, and PI-1918-3) in a one-atmosphere furnace under controlled oxygen fugacity after prior hydrothermal treatment at high pressure. For each sample, the diffusion coefficients for the full hydroxyl spectrum in the wavenumber range 3650-3200 cm⁻¹ were measured for diffusion parallel to the [100] and [001] crystallographic directions. Due to the relatively small signal-to-noise ratio for the integrated absorbance of the individual infrared bands, we separated the OH-bond related bands into two groups, 3650-3450 cm⁻¹ and 3450-3200 cm⁻¹, rather than analyzing each band separately. For similar reasons, we were not able to obtain robust chemical diffusivities for diffusion parallel to [010] for these samples.

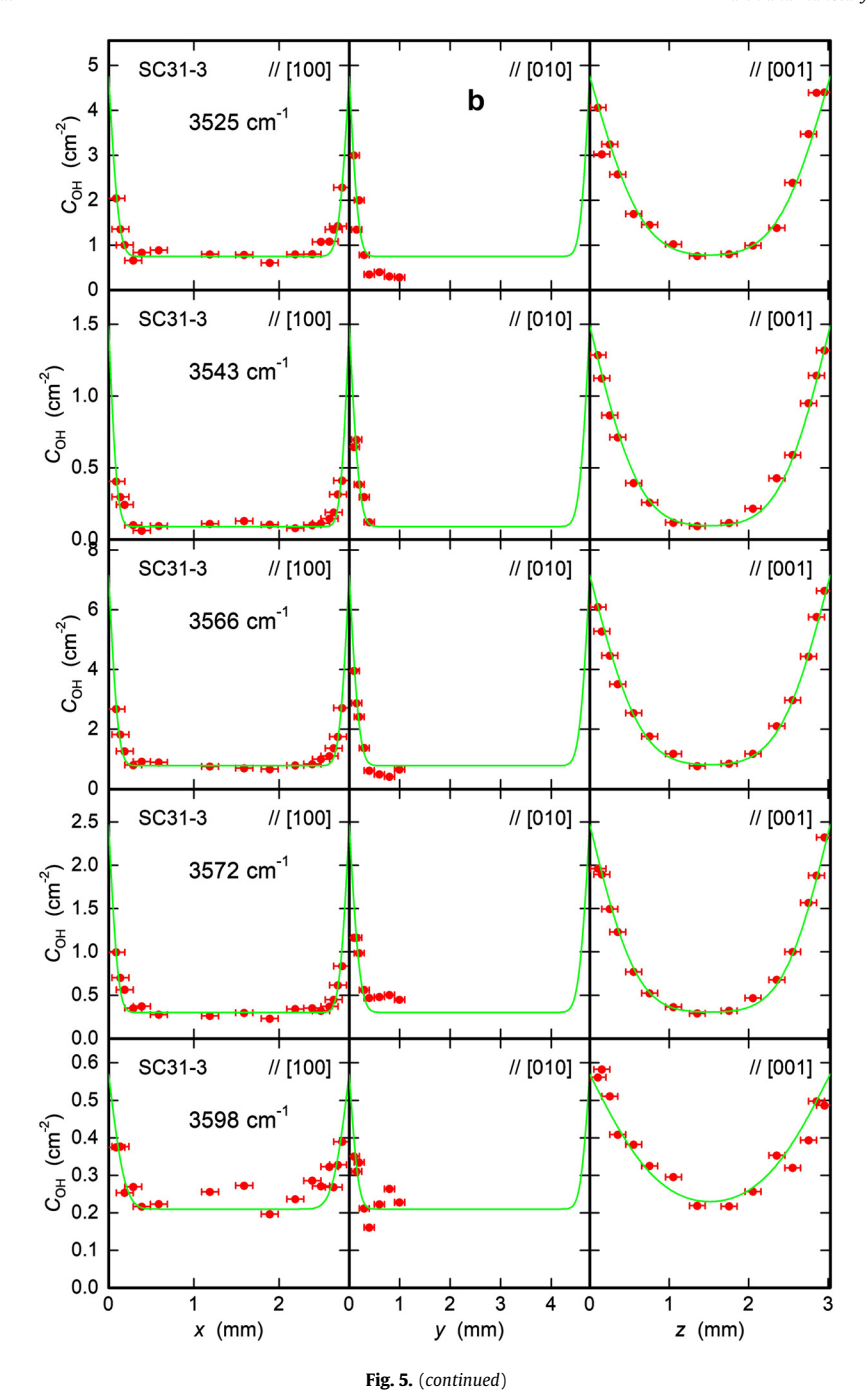


Table 2cChemical diffusivity data from dehydrogenation experiments for high and low wavenumber bands.

Sample	T (K)	t (h)	IR band (cm ⁻¹)	$\log \tilde{D}_s // [100]$ $(m^2 s^{-1})$	$\log \tilde{D}_s // [001]$ $(m^2 s^{-1})$
PI-1918-3	1191	20.0	All <3450 >3450	$\begin{array}{l} -13.4\pm0.1 \\ -13.4\pm0.2 \\ -13.42\pm0.07 \end{array}$	
PI-1914	1253	5.0	All <3450 >3450	$\begin{array}{l} -12.4\pm0.1 \\ -12.3\pm0.2 \\ -12.7\pm0.5 \end{array}$	$\begin{array}{c} -11.21\pm0.04 \\ -11.23\pm0.05 \\ -11.17\pm0.06 \end{array}$
PI-1918-1	1322	3.0	All <3450 >3450	$\begin{array}{l} -12.3\pm0.1 \\ -12.1\pm0.1 \\ -12.8\pm0.1 \end{array}$	-11.10 ± 0.04 -11.17 ± 0.06 -11.38 ± 0.05
PI-1918-2	1358	2.0	All <3450 >3450	$\begin{array}{l} -12.1\pm0.1 \\ -12.1\pm0.1 \\ -12.2\pm0.2 \end{array}$	$\begin{array}{c} -10.88 \pm 0.04 \\ -10.92 \pm 0.07 \\ -10.86 \pm 0.06 \end{array}$

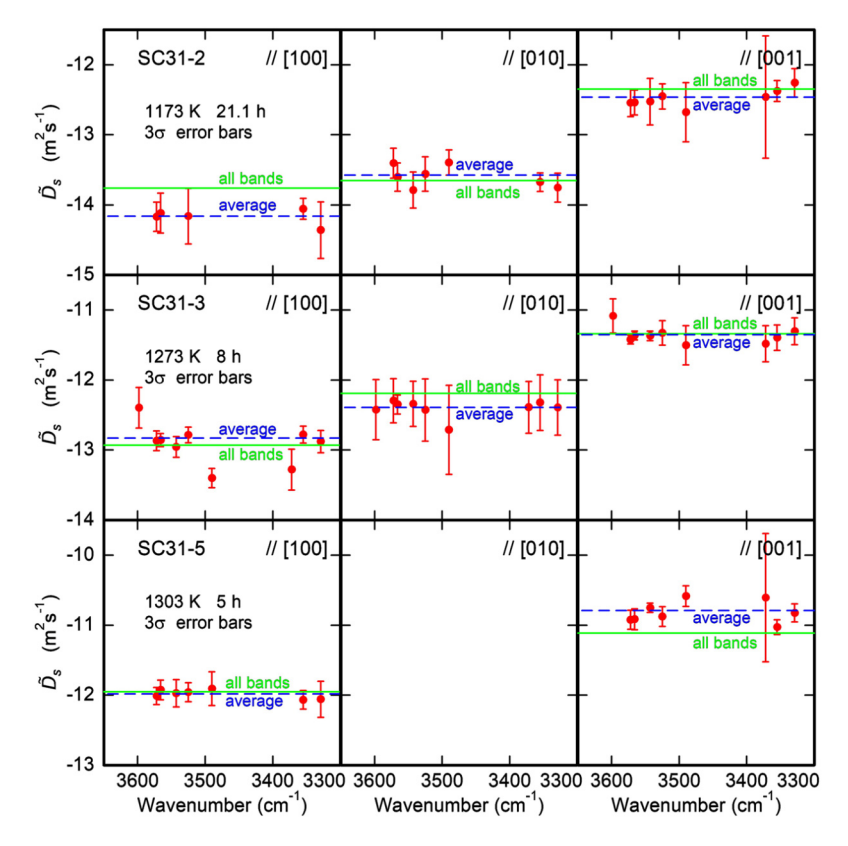


Fig. 6. Chemical diffusivities based on measurements of hydroxyl concentration as a function of position in olivine samples SC31-2, SC31-3, and SC31-5 after partial hydrogenation by the slow proton-vacancy coupled diffusion process. Each dashed line represents the average of the diffusivities determined for individual bands, while each solid line represents the diffusivity determined from the full infrared spectrum.

Chemical diffusivities were calculated from the diffusion profiles for the full hydroxyl spectrum and for each group of bands using Eq. (2) with C_0 and \tilde{D} as variables, and C_1 constrained at 0 due to the anhydrous environment during the dehydrogenation experiment. Dehydrogenation diffusion profiles are plotted in Fig. 7 for sample PI-1914 obtained from the full infrared spectrum and for each group of bands for diffusion parallel to [100] and [001]. The chemical diffusion data are listed in Table 2c and plotted in Fig. 8. For the dehydrogenation samples, the chemical diffusion coefficients calculated for the two groups of bands generally agree within experimental uncertainty.

5. Discussion

5.1. Diffusivities of water-derived defects

5.1.1. Proton-polaron exchange process

In Fig. 9, we plot chemical diffusivity versus temperature results from the present study for the fast diffusion process, along with published data from Mackwell and Kohlstedt (1990) and Kohlstedt and Mackwell (1998). The \times symbols are our measurements of diffusivity from the individual bands in the olivine spectrum, while the + symbols with 3σ error bars were determined from the full hydroxyl spectrum for each sample. The data from this study are consistent with our prior published analyses and indicate that changes in all the hydroxyl bands occur synchronously, arguing for a single diffusion process transporting protons from the exterior to the interior of each crystal. Most of the protons introduced during hydrogenation experiments react internally with newly formed or existing defects such as metal or silicon vacancies, resulting in hydroxyl bands reflecting the chemistry of the local environment associated with the defect species. Following our prior studies,

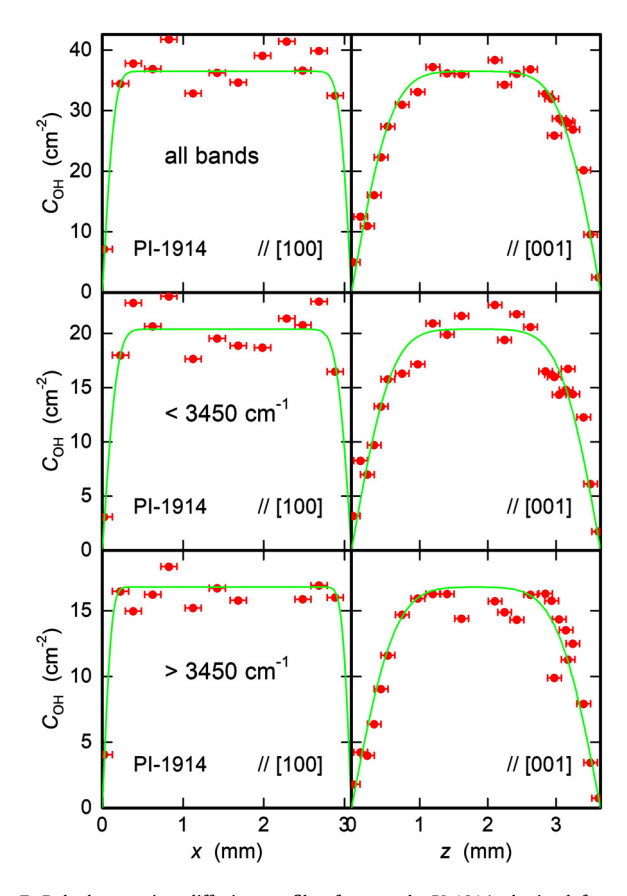


Fig. 7. Dehydrogenation diffusion profiles for sample PI-1914 obtained from the full infrared spectrum, from bands at wavenumbers $<3450~\rm{cm}^{-1}$, and bands at wavenumbers $>3450~\rm{cm}^{-1}$ for the diffusion parallel to [100] and [001].

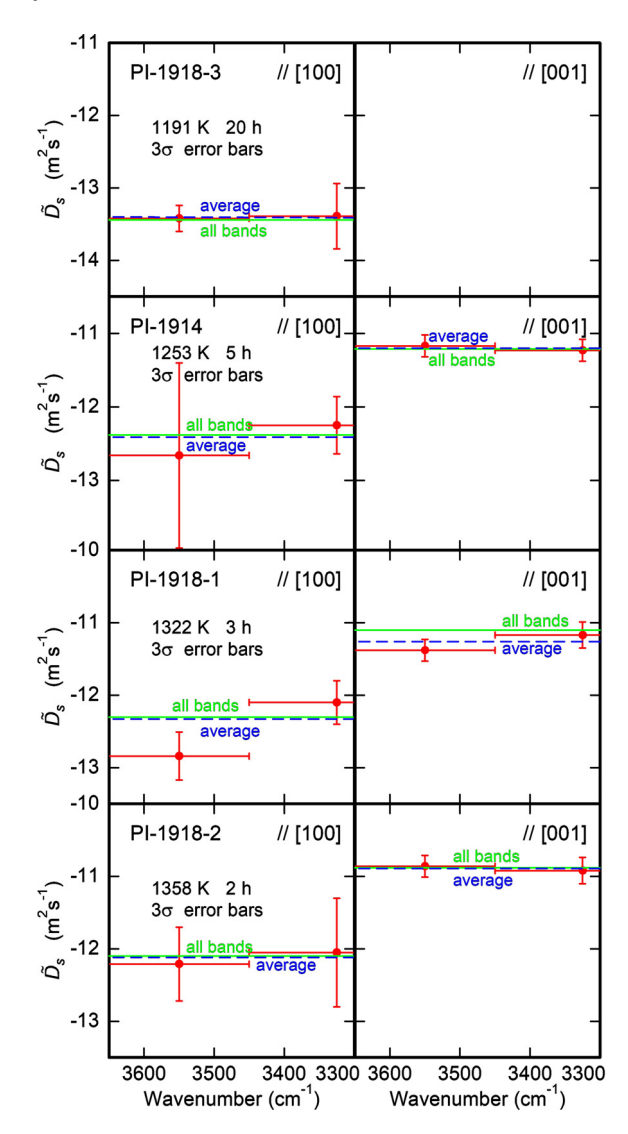


Fig. 8. Chemical diffusivities based on measurements of hydroxyl concentration as a function of position in olivine samples PI-1918-3, PI-1914, PI-1918-1, and PI-1918-2 after dehydrogenation of samples by the slow proton-vacancy coupled diffusion process. Each dashed line represents the average of the diffusivities for each band, while each solid line represents the measurement of hydroxyl concentration from the full spectrum.

we argue that the fast diffusion process involves counter-fluxes of interstitial protons and polarons with the chemical diffusion coefficient given in Eq. (3). In that case, since $D_p \gg D_H$, $D_H \approx 0.5 \tilde{D}_f$, allowing us to determine proton diffusion coefficients using the diffusion data for SC14-6 and SC16-4 in Table 2a. Since this new analysis only examined 2 of the 7 samples studied previously by Mackwell and Kohlstedt (1990) and Kohlstedt and Mackwell (1998) and the new data are quite consistent with the earlier results, we fit Arrhenius relations only to the data from the prior studies. These fits, plotted as the solid lines on Fig. 9, yielded

$$D_{\rm H}^a = 10^{-3.5 \pm 1.1} \exp\left(-\frac{145 \pm 25 \text{ kJ/mol}}{\text{RT}}\right) \text{m}^2 \text{s}^{-1},$$
 (5)

$$D_{\rm H}^b = 10^{-3.3 \pm 2.3} \exp\left(-\frac{184 \pm 52 \text{ kJ/mol}}{\text{RT}}\right) \text{m}^2 \text{s}^{-1},\tag{6}$$

$$D_{\rm H}^{b} = 10^{-3.3 \pm 2.3} \exp\left(-\frac{184 \pm 52 \text{ kJ/mol}}{\text{RT}}\right) \text{m}^{2} \text{s}^{-1}, \tag{6}$$

$$D_{\rm H}^{c} = 10^{-6.7 \pm 2.2} \exp\left(-\frac{105 \pm 43 \text{ kJ/mol}}{\text{RT}}\right) \text{m}^{2} \text{s}^{-1}, \tag{7}$$

where $D_{\rm H}^a$, $D_{\rm H}^b$, and $D_{\rm H}^c$ are the diffusion coefficients for hydrogen ions along [100], [010] and [001], respectively.

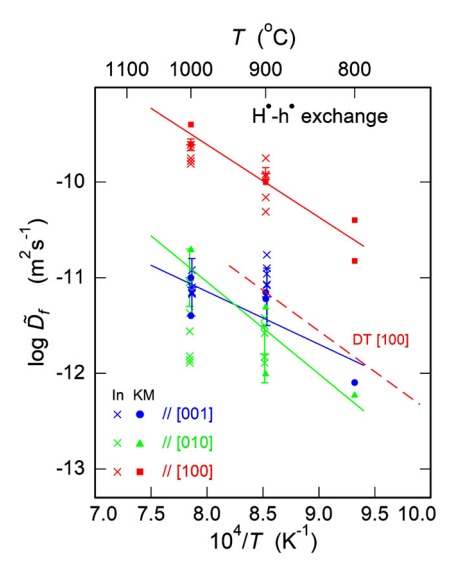


Fig. 9. Chemical diffusivities determined after short-duration hydrogenation experiments (In) that favored the fast diffusion process. The x symbols are measurements of average of the diffusivities for all the individual bands in the olivine spectrum, while the + symbols with 3σ error bars were determined from the full hydroxyl spectrum for each sample. By comparison, the filled symbols show the diffusivities determined in the prior study by Kohlstedt and Mackwell (1998) (KM) for each diffusion direction; the solid lines represent fits to their data. The dashed red line shows the chemical diffusivity parallel to [100] for hydrogen-deuterium exchange from Du Frane and Tyburczy (2012).

It should be noted that the chemical diffusivities determined from deuterium-hydrogen interdiffusion experiments on natural olivine by Du Frane and Tyburczy (2012), shown as the dashed red line in Fig. 9 for diffusion parallel to [100], yield hydrogen diffusivities a factor of \sim 7 slower than our calculations based on our fast diffusion experiments. This difference is unlikely to result from the higher pressure of their experiments.

5.1.2. Proton-vacancy coupled diffusion process

Chemical diffusivities based on hydroxyl profiles for SC31-2, SC31-3, SC31-5, PI-1918-3, PI-1914, PI-1918-1, and PI-1918-2 are provided in Table 2b, 2c and plotted versus inverse temperature in Fig. 10. The \times and Δ symbols are our measurements of chemical diffusivity for the individual bands in the natural olivine spectrum for the hydrogenation (In) and dehydrogenation (Out) experiments, respectively, while the + symbols with 3σ error bars were determined from the full hydroxyl spectrum for each sample. The similarities of the hydrogenation and dehydrogenation data are consistent with operation of the same diffusion process in both types of experiment. The slower rate of diffusion and differences in anisotropy of diffusion between these results and those for the proton-polaron exchange process clearly demonstrate the operation of two different diffusion processes for hydrogen transport. We argue, as did Kohlstedt and Mackwell (1998) and Demouchy and Mackwell (2006), that this slower diffusion process involves coupled diffusion of interstitial protons and metal vacancies.

The chemical diffusion coefficient for the coupled diffusion of interstitial protons and metal vacancies is described in terms of the proton and metal vacancy diffusivities by Eq. (4). Since $D_{\rm H} \gg D_{\rm V_{Me}}$, $D_{V_{Ma}} \approx \frac{1}{3} \tilde{D}_s$, allowing us to determine metal vacancy diffusion coefficients for this suite of samples. The metal vacancy diffusivities determined from the full hydroxyl spectrum for each diffusion direction of our samples are plotted in Fig. 11. A fit of the Arrhenius relation to our metal vacancy diffusivity data for each diffusion direction based on results from both hydrogenation experiments and dehydrogenation experiments yields

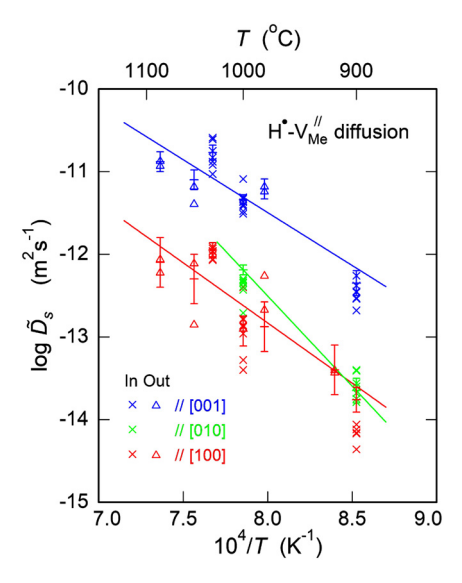


Fig. 10. Chemical diffusivities determined from samples after longer-duration hydrogenation (In) and dehydrogenation (Out) experiments that favored the slow proton-vacancy coupled diffusion process. The \times symbols are diffusivities from individual bands in the infrared spectrum due to hydrogenation for each diffusion direction, while the Δ symbols are diffusivities due to dehydrogenation. The + symbols with 3σ error bars show diffusivities that were determined from the full hydroxyl spectrum for each sample; the solid lines illustrate least squares regression fits to the diffusivities for the full hydroxyl spectra but not the individual bands.

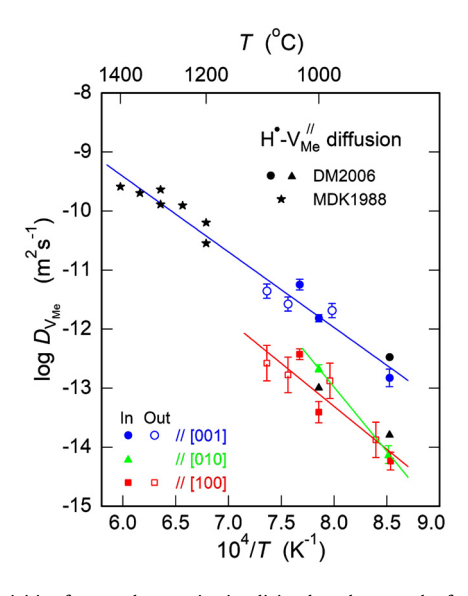


Fig. 11. Diffusivities for metal vacancies in olivine based on results from this study (colored open and closed symbols) after hydrogenation (In) and dehydrogenation (Out) experiments, results from Demouchy and Mackwell (2006) (DM2006: black closed circles and triangles), and results from Mackwell et al. (1988) (MDK1988: black stars). The solid lines are the same as in Fig. 10, allowing for the factor of 3 difference between chemical diffusivity and metal vacancy diffusivity.

 $D_{V_{Me}}^{a}(dehydrogenation + hydrogenation)$

$$= 10^{-1.2 \pm 2.5} \exp \left(-\frac{279 \pm 60 \text{ kJ/mol}}{RT} \right) \text{m}^2 \text{s}^{-1},$$

and

 $D_{V_{Me}}^{c}(dehydrogenation + hydrogenation)$

$$= 10^{-1.3 \pm 2.2} \exp\left(-\frac{245 \pm 54 \text{ kJ/mol}}{RT}\right) \text{ m}^2 \text{ s}^{-1}.$$

Since only 2 points constrained the metal vacancy diffusivity for diffusion parallel to [010], the fit is not very robust and thus is not quoted here. Also plotted on this figure are metal vacancy diffusivities from Demouchy and Mackwell (2006) based on similar experiments of hydrogen diffusion and from Mackwell et al. (1988) based on re-equilibration rates of natural olivine single crystals after changes in oxygen fugacity during deformation experiments. Our data are consistent with those of Demouchy and Mackwell (2006), although we did not use their diffusivity for 1173 K due to scatter in the hydroxyl concentration profile. That the extrapolation of the Arrhenius fit for the [001] data to higher temperatures aligns so well with the metal vacancy diffusivities of Mackwell et al. (1988) determined by a totally different method gives confidence in the assignment of the proton-vacancy coupled diffusion as the operative defect diffusion process.

5.2. Comparison to prior studies

Padrón-Navarta et al. (2014) reported that diffusivities associated with different hydrous defects in synthetic forsterite and Tidoped forsterite differ by several orders of magnitude. The fastest species linked to the band at 3220 cm⁻¹ was assigned to hydrogen associated with magnesium vacancies; the slower species linked to the bands at 3572 and 3525 cm⁻¹ was interpreted as hydrogen associated with titanium defects; and the slowest species associated with bands at 3613, 3566, and 3542 cm⁻¹ was assigned to hydrogen associated with silicon vacancies.

Further to these observations, Jollands et al. (2016, 2019) note that their results for dehydrogenation in synthetic forsterite and natural olivine are all consistent with the predominant diffusion process for hydrogen involving protons and metal vacancies combined with inter-site reactions in which protons progressively leave largely immobile trapping sites and move into a faster transport pathway, such as coupled diffusion with metal vacancies. Our results are consistent with these observations, clearly demonstrating that, after an initial fast exchange of protons and polarons, a single diffusion process involving coupled diffusion of interstitial protons and metal vacancies dominates. The anisotropies in diffusion kinetics that we observed are also consistent with those of these prior studies. As noted in Jollands et al. (2019), variations exist in rates of diffusion measured in the various studies that need to be resolved, but the consistency of results in terms of the diffusion mechanism gives some confidence in the utility of these studies for application to processes in Earth's interior.

5.3. Application to assent rate of mantle xenoliths

Hydroxyl profiles have been measured for olivine xenocrysts and olivine grains in mantle xenoliths due to dehydrogenation during ascent from their source regions (e.g., Demouchy et al., 2006; Peslier and Luhr, 2006; Peslier et al., 2008, 2015; Denis et al., 2013; Hilchie et al., 2014; Ferriss et al., 2018; Barth et al., 2019; Newcombe et al., 2020). Generally, these samples exhibit spectral features common to infrared spectra from mantle-derived olivine (Miller et al., 1987; Ingrin and Skogby, 2000) including bands located at around 3572, 3525, 3353, and 3330 cm⁻¹. Results from the present study have demonstrated that all the major bands in natural San Carlos olivine crystals exhibit similar rates of change during dehydrogenation, suggestive of a common mechanism of hydrogen transport. In addition, the similarity between the diffusivities obtained from hydrogenation and dehydrogenation experiments validates the use of the diffusivities obtained from hydrogenation experiments in our earlier publications to calculate the ascent rates of the host magma carrying olivine xenocrysts or olivine-bearing xenoliths. While an understanding of the nature and mobility of hydrogen-associated point defects in natural olivine remains incomplete, the identification of a single key mechanism for hydrogenation and dehydrogenation provides confidence

in the calculations of ascent rates for mantle xenocrysts and xeno-

CRediT authorship contribution statement

Yang (Will) Li: Conceptualization, Formal analysis, Investigation, Methodology, Software, Visualization, Writing – original draft. Stephen J. Mackwell: Conceptualization, Formal analysis, Investigation, Resources, Validation, Writing – review & editing. David L. Kohlstedt: Conceptualization, Data curation, Formal analysis, Funding acquisition, Investigation, Methodology, Project administration, Supervision, Writing – review & editing.

Declaration of competing interest

The authors declare that they have no known competing financial interests or personal relationships that could have appeared to influence the work reported in this paper.

Acknowledgements

We acknowledge technical support from Mark Zimmerman in the performance of the experiments and Jed Mosenfelder for help with the infrared spectroscopy and for valuable discussions. The manuscript was improved by insightful comments by an anonymous reviewer. This work was supported by grant EAR-1755805 from the National Science Foundation.

References

- Bai, Q., Kohlstedt, D.L., 1992. Substantial hydrogen solubility in olivine and implications for water storage in the mantle. Nature 357, 672–674. https://doi.org/10. 1038/357672a0
- Bai, Q., Kohlstedt, D.L., 1993. Effects of chemical environment on the solubility and incorporation mechanism for hydrogen in olivine. Phys. Chem. Miner. 19, 460–471. https://doi.org/10.1007/BF00203186.
- Balan, E., Ingrin, J., Delattre, S., Kovács, I., Blanchard, M., 2011. Theoretical infrared spectrum of OH-defects in forsterite. Eur. J. Mineral. 23, 285–292. https://doi. org/10.1127/0935-1221/2011/0023-2090.
- Barth, A., Newcombe, M., Plank, T., Gonnermann, H., Hajimirza, S., Soto, G.J., Saballos, A., Hauri, E., 2019. Magma decompression rate correlates with explosivity at basaltic volcanoes constraints from water diffusion in olivine. J. Volcanol. Geotherm. Res. 387, 106664. https://doi.org/10.1016/j.jvolgeores.2019.106664.
- Beran, A., Putnis, A., 1983. A model of the OH positions in olivine, derived from infrared-spectroscopic investigations. Phys. Chem. Miner. 9, 57–60. https://doi. org/10.1007/BF00308148.
- Berry, A.J., Hermann, J., O'Neill, H.S.C., Foran, G.J., 2005. Fingerprinting the water site in mantle olivine. Geology 33, 869–872. https://doi.org/10.1130/G21759.1.
- Berry, A.J., O'Neill, H.S.C., Hermann, J., Scott, D.R., 2007. The infrared signature of water associated with trivalent cations in olivine. Earth Planet. Sci. Lett. 261, 134–142. https://doi.org/10.1016/j.epsl.2007.06.021.
- Braithwaite, J.S., Wright, K., Catlow, C.R.A., 2003. A theoretical study of the energetics and IR frequencies of hydroxyl defects in forsterite. J. Geophys. Res. 108, 2234. https://doi.org/10.1029/2002JB002126.
- Brodholt, J.P., Refson, K., 2000. An ab initio study of hydrogen in forsterite and a possible mechanism for hydrolytic weakening. J. Geophys. Res. 105, 18977–18982. https://doi.org/10.1029/2000/B900057.
- Carslaw, H.S., Jaeger, J.C., 1959. Conduction of Heat in Solids. Clarendon Press, Oxford.
- Chakraborty, S., 1997. Rates and mechanisms of Fe-Mg interdiffusion in olivine at 980°-1300°C. J. Geophys. Res. 102, 12317–12331. https://doi.org/10.1029/97IB00208.
- Chakraborty, S., 2010. Diffusion coefficients in olivine, wadsleyite and ringwoodite. Rev. Mineral. Geochem. 72, 603–639. https://doi.org/10.2138/rmg.2010.72.13.
- Costa, F., Chakraborty, S., 2008. The effect of water on Si and O diffusion rates in olivine and implications for transport properties and processes in the upper mantle. Phys. Earth Planet. Inter. 166, 11–29. https://doi.org/10.1016/j.pepi.2007. 10.006
- Crépisson, C., Bureau, H., Blanchard, M., Ingrin, J., Balan, E., 2014. Theoretical infrared spectrum of partially protonated cationic vacancies in forsterite. Eur. J. Mineral. 26, 203–210. https://doi.org/10.1127/0935-1221/2014/0026-2366.
- Demouchy, S., Alard, O., 2021. Hydrogen, trace, and ultra-trace element distribution in natural olivines. Contrib. Mineral. Petrol. 176, 26. https://doi.org/10.1007/s00410-021-01778-5.

- Demouchy, S., Mackwell, S., 2003. Water diffusion in synthetic iron-free forsterite. Phys. Chem. Miner. 30, 486–494. https://doi.org/10.1007/s00269-003-0342-2.
- Demouchy, S., Mackwell, S., 2006. Mechanisms of hydrogen incorporation and diffusion in iron-bearing olivine. Phys. Chem. Miner. 33, 347–355. https://doi.org/10.1007/s00269-006-0081-2.
- Demouchy, S., Jacobsen, S.D., Gaillard, F., Stern, C.R., 2006. Rapid magma ascent recorded by water diffusion profiles in mantle olivine. Geology 34, 429–432. https://doi.org/10.1130/G22386.1.
- Denis, C.M., Demouchy, S., Shaw, C.S., 2013. Evidence of dehydration in peridotites from Eifel volcanic field and estimates of the rate of magma ascent. J. Volcanol. Geotherm. Res. 258, 85–99. https://doi.org/10.1016/j.jvolgeores.2013.04.010.
- Dohmen, R., Becker, H-W., Chakraborty, S., 2007. Fe–Mg diffusion in olivine I: experimental determination between 700 and 1,200°C as a function of composition, crystal orientation and oxygen fugacity. Phys. Chem. Miner. 34, 389–407. https://doi.org/10.1007/s00269-007-0157-7.
- Dohmen, R., Chakraborty, S., 2007. Fe–Mg diffusion in olivine II: point defect chemistry, change of diffusion mechanisms and a model for calculation of diffusion coefficients in natural olivine. Phys. Chem. Miner. 34, 409–430. https://doi.org/10.1007/s00269-007-0185-3.
- Du Frane, W.L., Tyburczy, J.A., 2012. Deuterium-hydrogen exchange in olivine: implications for point defects and electrical conductivity. Geochem. Geophys. Geosyst. 13, Q03004. https://doi.org/10.1029/2011GC003895.
- Ferriss, E., Plank, T., Newcombe, M., Walker, D., Hauri, E., 2018. Rates of dehydration of olivines from San Carlow and Kilauea Iki. Geochim. Cosmochim. Acta 242, 165–190. https://doi.org/10.1016/j.gca.2018.08.050.
- Ferriss, E., Plank, T., Walker, D., Nettles, M., 2015. The whole-block approach to measuring hydrogen diffusivity in nominally anhydrous minerals. Am. Mineral. 100, 837–851. https://doi.org/10.2138/am-2015-4947.
- Gaetani, G.A., O'Leary, J.A., Koga, K.T., Hauri, E.H., Rose-Koga, E.F., Monteleone, B.D., 2014. Hydration of mantle olivine under variable water and oxygen fugacity conditions. Contrib. Mineral. Petrol. 167, 1–14. https://doi.org/10.1007/s00410-014-0965-y.
- Green, D.H., Hibberson, W.O., Kovács, I., Rosenthal, A., 2010. Water and its influence on the lithosphere-asthenosphere boundary. Nature 467, 448–451. https://doi. org/10.1038/nature09369.
- He, Y., Dai, L., Kim, D.Y., Li, H., Karato, S-I., 2021. Thermal ionization of hydrogen in hydrous olivine with enhanced and anisotropic conductivity. J. Geophys. Res. 126, e2021|B022939. https://doi.org/10.1029/2021|B022939.
- Hilchie, L., Fedortchouk, Y., Matveev, S., Kopylova, M.G., 2014. The origin of high hydrogen content in kimberlitic olivine: evidence from hydroxyl zonation in olivine from kimberlites and mantle xenoliths. Lithos 202, 429–441. https:// doi.org/10.1016/i.lithos.2014.06.010.
- Hirschmann, M.M., 2006. Water, melting, and the deep earth H₂O cycle. Annu. Rev. Earth Planet. Sci. 34, 629–653. https://doi.org/10.1146/annurev.earth.34.031405. 125211.
- Ingrin, J., Skogby, H., 2000. Hydrogen in nominally anhydrous upper-mantle minerals concentration levels and implications. Eur. J. Mineral. 12, 543–570. https://doi.org/10.1127/0935-1221/2000/0012-0543.
- Jacobsen, S.D., Jiang, F., Mao, Z., Duffy, T.S., Smyth, J.R., Holl, C.M., Frost, D.J., 2008. Effects of hydration on the elastic properties of olivine. Geophys. Res. Lett. 35, L14303. https://doi.org/10.1029/2008GL034398.
- Jollands, M.C., Padrón-Navarta, J.A., Hermann, J., O'Neill, H.S.C., 2016. Hydrogen diffusion in Ti-doped forsterite and the preservation of metastable point defects. Am. Mineral. 101, 1571–1583. https://doi.org/10.2138/am-2016-5568.
- Jollands, M.C., Kempf, E., Hermann, J., Müntener, O., 2019. Coupled inter-site reaction and diffusion: rapid dehydrogenation of silicon vacancies in natural olivine. Geochim. Cosmochim. Acta 262, 220–242. https://doi.org/10.1016/j.gca.2019.07.
- Jollands, M.C., Zhukova, I., O'Neill, H.S.C., Hermann, J., 2020. Mg diffusion in forsterite from 1250-1600 °C. Am. Mineral. 105, 525–537. https://doi.org/10.2138/am-2020-7286.
- Karato, S-I., 2003. Mapping water content in upper mantle. In: Eiler, J. (Ed.), Inside the Subduction Factory. In: Geophys. Monogr., vol. 138. AGU, Washington, DC, pp. 135–152.
- Karato, S-I., 2006. Influence of hydrogen-related defects on the electrical conductivity and plastic deformation of mantle minerals: a critical review. In: Jacobsen, S.D., van der Lee, S. (Eds.), Earth's Deep Water Cycle. In: Geophys. Monogr., vol. 168. AGU, Washington, DC, pp. 113–129.
- Karato, S-I., 2010. Rheology of the deep upper mantle and its implications for the preservation of the continental roots: a review. Tectonophysics 481, 82–98. https://doi.org/10.1016/j.tecto.2009.04.011.
- Karato, S-I., 2011. Water distribution across the mantle transition zone and its implications for global material circulation. Earth Planet. Sci. Lett. 301, 413–423. https://doi.org/10.1016/j.epsl.2010.11.038.
- Kohlstedt, D., Keppler, H., Rubie, D., 1996. Solubility of water in the α , β and Υ phases of (Mg, Fe)₂SiO₄. Contrib. Mineral. Petrol. 123, 345–357. https://doi.org/10.1007/s004100050161.
- Kohlstedt, D.L., 2006. The role of water in high-temperature rock deformation. Rev. Mineral. Geochem. 62, 377–396. https://doi.org/10.2138/rmg.2006.62.16.

- Kohlstedt, D.L., Mackwell, S.J., 1998. Diffusion of hydrogen and intrinsic point defects in olivine. Z. Phys. Chem. 207, 147–162. https://doi.org/10.1524/zpch.1998.207. Part 1 2.147.
- Kovács, I., O'Neill, H.S.C., Hermann, J., Hauri, E.H., 2010. Site-specific infrared OH absorption coefficients for water substitution into olivine. Am. Mineral. 95, 292-299. https://doi.org/10.2138/am.2010.3313.
- Kröger, F., Vink, H., 1956. Relations between the concentrations of imperfections in crystalline solids. Solid State Phys. 3, 307–435.
- Le Losq, C., Jollands, M.C., Tollan, P.M.E., Hawkins, R., O'Neill, H.S.C., 2019. Point defect populations of forsterite revealed by two-stage metastable hydroxylation experiments. Contrib. Mineral. Petrol. 174, 53. https://doi.org/10.1007/s00410-019-1590-6.
- Lemaire, C., Kohn, S., Brooker, R., 2004. The effect of silica activity on the incorporation mechanisms of water in synthetic forsterite: a polarised infrared spectroscopic study. Contrib. Mineral. Petrol. 147, 48–57. https://doi.org/10.1007/ s00410-003-0539-x.
- Libowitzky, E., Beran, A., 1995. OH defects in forsterite. Phys. Chem. Miner. 22, 387–392. https://doi.org/10.1007/BF00213336.
- Mackwell, S., Dimos, D., Kohlstedt, D.L., 1988. Transient creep of olivine: point-defect relaxation times. Philos. Mag. A 57, 779–789. https://doi.org/10.1080/01418618808209920.
- Mackwell, S.J., Kohlstedt, D.L., 1990. Diffusion of hydrogen in olivine: implications for water in the mantle. J. Geophys. Res. 95, 5079–5088. https://doi.org/10.1029/JB095iB04p05079.
- Mackwell, S., Kohlstedt, D., Paterson, M., 1985. The role of water in the deformation of olivine single crystals. J. Geophys. Res. 90, 11,319–11,333. https://doi.org/10.1029/IB090iB13p11319.
- Matveev, S., O'Neill, H.S.C., Ballhaus, C., Taylor, W., Green, D., 2001. Effect of silica activity on OH⁻ IR spectra of olivine: implications for low-a_{SiO2} mantle meta-somatism. J. Petrol. 42, 721–729. https://doi.org/10.1093/petrology/42.4.721.
- Miller, G.H., Rossman, G.R., Harlow, G.E., 1987. The natural occurrence of hydroxide in olivine. Phys. Chem. Miner. 14, 461–472. https://doi.org/10.1007/BF00628824.
- Mosenfelder, J.L., Deligne, N.I., Asimow, P.D., Rossman, G.R., 2006. Hydrogen incorporation in olivine from 2–12 GPa. Am. Mineral. 91, 285–294. https://doi.org/10.2138/am.2006.1943.
- Nakamura, A., Schmalzried, H., 1983. On the nonstoichiometry and point defects of olivine. Phys. Chem. Miner. 10, 27–37. https://doi.org/10.1007/BF01204323.
- Newcombe, M., Plank, T., Barth, A., Asimov, P.D., Hauri, E., 2020. Water-in-olivine magma ascent chronometry: every crystal is a clock. J. Volcanol. Geotherm. Res. 398, 106872. https://doi.org/10.1016/j.jvolgeores.2020.106872.
- Padrón-Navarta, J.A., Hermann, J., O'Neill, H.S.C., 2014. Site-specific hydrogen diffusion rates in forsterite. Earth Planet. Sci. Lett. 392, 100–112. https://doi.org/10.1016/j.epsl.2014.01.055.
- Padrón-Navarta, J.A., Hermann, J., 2017. A subsolidus olivine water solubility equation for the Earth's upper mantle. J. Geophys. Res. 122, 9862–9880. https://doi.org/10.1002/2017JB014510.
- Paterson, M., 1990. Rock deformation experimentation. In: Duba, A.G., Durham, W.B., Handin, J.W., Wang, H.F. (Eds.), The Brittle-Ductile Transition in Rocks. In: Geophys. Monogr., vol. 56. AGU, Washington, DC, pp. 187–194.

- Peslier, A.H., 2010. A review of water contents of nominally anhydrous natural minerals in the mantles of Earth, Mars and the Moon. J. Volcanol. Geotherm. Res. 197, 239–258. https://doi.org/10.1016/j.jvolgeores.2009.10.006.
- Peslier, A.H., Luhr, J.F., 2006. Hydrogen loss from olivines in mantle xenoliths from Simcoe (USA) and Mexico: mafic alkalic magma ascent rates and water budget of the sub-continental lithosphere. Earth Planet. Sci. Lett. 242, 302–319. https://doi.org/10.1016/j.epsl.2005.12.019.
- Peslier, A.H., Woodland, A.B., Wolff, J.A., 2008. Fast kimberlite ascent rates estimated from hydrogen diffusion profiles in xenolithic mantle olivines from southern Africa. Geochim. Cosmochim. Acta 72, 2711–2722. https://doi.org/10.1016/j.gca. 2008.03.019.
- Peslier, A.H., Bizimis, M., Matney, M., 2015. Water disequilibrium in olivines from Hawaiian peridotites: recent metasomatism, H diffusion and magma ascent rates. Geochim. Cosmochim. Acta 154, 98–117. https://doi.org/10.1016/j.gca. 2015.01.030.
- Sato, H., 1986. High temperature a.c. electrical properties of olivine single crystal with varying oxygen partial pressure: implications for the point defect chemistry. Phys. Earth Planet. Inter. 41, 269–282. https://doi.org/10.1016/0031-9201(86)90006-3.
- Tollan, P.M.E., Smith, R., O'Neill, H.S.C., Hermann, J., 2017. The responses of the four main substitution mechanisms of H in olivine to H₂O activity at 1050 °C and 3 GPa. Prog. Earth Planet. Sci. 4. 14. https://doi.org/10.1186/s40645-017-0128-7.
- Tollan, P.M.E., O'Neill, H.S.C., Hermann, J., 2018. The role of trace elements in controlling H incorporation in San Carlos olivine. Contrib. Mineral. Petrol. 173, 89. https://doi.org/10.1007/s00410-018-1517-7.
- Tsai, T-L., Dieckmann, R., 1997. Point defects and transport of matter and charge in olivines (Fe_xMg_{1-x})₂SiO₄. Mater. Sci. Forum 239, 399–402. https://doi.org/10.4028/www.scientific.net/MSF.239-241.399.
- Tsai, T-L., Dieckmann, R., 2002. Variation of the oxygen content and point defects in olivines(Fe_xMg_{1-x})₂SiO₄, $0.2 \le x \le 1.0$. Phys. Chem. Miner. 29, 680–694. https://doi.org/10.1007/s00269-002-0283-1
- Umemoto, K., Wentzcovitch, R.M., Hirschmann, M.M., Kohlstedt, D.L., Withers, A., 2011. A first-principles investigation of hydrous defects and IR frequencies in forsterite: the case for Si vacancies. Am. Mineral. 96, 1475–1479. https://doi. org/10.2138/am.2011.3720.
- Walker, A., Hermann, J., Berry, A., O'Neill, H.S.C., 2007. Three water sites in upper mantle olivine and the role of titanium in the water weakening mechanism. J. Geophys. Res. 112, B05211. https://doi.org/10.1029/2006/B004620.
- Withers, A.C., Hirschmann, M.M., 2008. Influence of temperature, composition, silica activity and oxygen fugacity on the H₂O storage capacity of olivine at 8 GPa. Contrib. Mineral. Petrol. 156, 595–605. https://doi.org/10.1007/s00410-008-0303.3
- Wright, K., Catlow, C.R.A., 1994. A computer simulation study of (OH) defects in olivine. Phys. Chem. Miner. 20, 515–518. https://doi.org/10.1007/BF00203222.